Applied Chemical Engineering (2026) Volume 9 Issue 3 ISSN: 2578-2010 (O)
doi: 10.59429/ace.v9i3.5987

RESEARCH ARTICLE

Synthesis and Characterization of Nanocomposites for ZnO and Application in Solar Cells

Ali S*, M, Kuba, Amer M. J. AL - Shammari, Manal F.M. AL-Khakani

Chemistry Department, College of Science, University of Kufa, Iraq

***Corresponding author:** Ali S, ali22220189@gmail.com

ABSTRACT

Dye-sensitized solar cells (DSSCs) were fabricated using ZnO, ZnO/TiO_2, and ZnO/NiO nanoparticles and nanocomposites prepared via the co-deposition method. The synthesized materials were employed as photoelectrodes and sensitized with two dyes, namely Brilliant Blue FCF (E133) and red cabbage extract, to investigate their influence on the photovoltaic performance of DSSCs. The structural, morphological, surface, and optical properties of the prepared materials were characterized using X-ray diffraction (XRD), scanning electron microscopy (SEM), transmission electron microscopy (TEM), Fourier transform infrared spectroscopy (FTIR), Brunauer–Emmett–Teller (BET) surface area analysis, and optical measurements. The characterization results confirmed the successful synthesis of nanostructured metal oxide materials and revealed significant differences in crystallinity, morphology, surface area, and optical behavior among the investigated samples. The photovoltaic performance of the fabricated DSSCs was evaluated from current density–voltage (J–V) measurements under an illumination intensity of 22.53 mW cm^{-2}. The photovoltaic parameters, including open-circuit voltage (Voc), short-circuit current density (Jsc), fill factor (FF), maximum output power (Pmax), and power conversion efficiency (η), were determined and compared. The results demonstrated that DSSCs sensitized with Brilliant Blue FCF exhibited superior photovoltaic performance compared with those sensitized with red cabbage extract. The highest photovoltaic performance was achieved for the ZnO photoelectrode sensitized with Brilliant Blue FCF dye, yielding a Voc of 0.87 V, a Jsc of 1.56 mA/cm^2, a fill factor of 0.6406, a maximum output power of 1.3933 mW, and a power conversion efficiency of 3.865%. The enhanced photovoltaic performance was attributed to the favorable structural and surface characteristics of the ZnO photoelectrode, including its crystallinity, morphology, and available surface area, which promoted efficient dye adsorption, light harvesting, and charge transport. These findings highlight the potential of ZnO-based photoelectrodes and appropriate dye selection for improving DSSC performance and provide valuable insights into the relationship between material properties and photovoltaic behavior.

Keywords: Semiconductors, photoelectrodes, DSSC construction, nanochemical production, and conversion efficiency.

ARTICLE INFO

Received: 20 April 2026
Accepted: 01 June 2026
Available online: 28 September 2026

COPYRIGHT

Copyright © 2025 by author(s).
Applied Chemical Engineering is published by Arts and Science Press Pte. Ltd. This work is licensed under the Creative Commons Attribution-NonCommercial 4.0 International License (CC BY 4.0).
https://creativecommons.org/licenses/by/4.0/

1. Introduction

Concerns related to climate change, greenhouse gas emissions, and the continuously increasing global energy demand have become more critical as the world's population continues to grow [1,2]. Due to their low cost, simple fabrication processes, abundant raw materials, and scalability, third-generation photovoltaic technologies—such as dye-sensitized solar cells (DSSCs) [3], organic solar cells (OSCs) [4], and perovskite solar cells (PSCs) [5,6]—have attracted significant scientific attention. Among these technologies, DSSCs are particularly attractive for portable electronic applications owing to their lightweight, compact, and flexible architectures [7–9]. In addition, DSSCs exhibit efficient performance under low-light conditions,

making them suitable for energy harvesting in wireless sensors and Internet of Things (IoT) devices [7,10–12]. In order to improve the photovoltaic performance, charge transport properties, and long-term stability of DSSCs, recent research has focused on the development of novel materials and advanced device architectures [13–22]. To enhance electron transport and suppress charge recombination, a variety of nanostructured materials have been investigated, including doped TiO_2, graphene derivatives, carbon-based materials, and metal oxide heterostructures. For example, sulfur-doped TiO_2 photoanodes have demonstrated improved DSSC efficiency due to enhanced charge transport and reduced trap-state density. Similarly, defect-engineered MoC/MoO_2 nanostructures embedded within N-doped carbon frameworks have exhibited improved electrocatalytic activity and stability. In addition, graphene-based and other carbonaceous counter electrodes have emerged as promising low-cost alternatives to platinum (Pt) electrodes due to their high electrical conductivity and catalytic performance. These results suggest that improving DSSC performance largely depends on heterostructure engineering, surface modification, and defect control. Among the available synthesis techniques, chemical precipitation has attracted considerable attention due to its simplicity, rapid processing, low cost, and ability to produce high-purity nanomaterials with controlled properties. The comparative analysis of chemically precipitated mixed-oxide nanocomposites under low-intensity illumination using natural dye sensitizers has received little attention, despite the numerous studies reported on ZnO-, TiO_2-, and NiO-based nanomaterials for DSSC applications [23,24]. The novelty of the present work lies in the systematic synthesis and comparative analysis of ZnO, TiO_2, NiO, and their binary and ternary nanocomposites prepared via an economical chemical precipitation method [29], as well as their incorporation into DSSC devices using natural dyes and carbon-based counter electrodes. The present study establishes a direct relationship between nanocomposite composition, structural characteristics, crystallite properties, surface-related dye adsorption capability [28], and photovoltaic performance, in contrast to earlier studies that primarily focused on single-metal oxide systems or employed costly sensitizers and counter electrodes. In addition, this work demonstrates how mixed nanostructured oxides can enhance charge transport pathways and suppress electron–hole recombination [26,27], thereby improving DSSC efficiency under cost-effective fabrication conditions. Specifically, the ZnO/TiO_2 nanocomposite was designed to combine the superior chemical stability and high dye adsorption capacity of TiO_2 with the high electron mobility of ZnO, thereby potentially enhancing electron transport and reducing charge recombination losses in DSSCs [30]. Overall, this integrated approach offers a viable pathway toward the development of cost-effective, environmentally friendly, and scalable DSSC systems for sustainable energy applications [25].

2. Procedure

2.1. Synthesis of Zinc Oxide Nanoparticles Using Precipitation

Zinc oxide (ZnO) nanoparticles were synthesized using the chemical precipitation method. Zinc chloride ($ZnCl_2$) and sodium hydroxide (NaOH) were used as precursor materials. All chemicals were dissolved in deionized water prior to synthesis. A 0.1 M $ZnCl_2$ solution was prepared by dissolving zinc chloride in 100 mL of deionized water and stirring continuously with a magnetic stirrer for 30 min to ensure complete dissolution. Simultaneously, a 0.2 M NaOH solution was prepared by dissolving sodium hydroxide in 100 mL of deionized water under continuous stirring for the same duration.

The NaOH solution was then added dropwise to the $ZnCl_2$ solution under constant magnetic stirring until the pH of the reaction mixture reached 12. As a result, a white precipitate of zinc hydroxide ($Zn(OH)_2$) was formed. The precipitate was collected by centrifugation and repeatedly washed with deionized water and ethanol to remove residual impurities. Subsequently, the obtained product was dried in an electric oven at 80°C and then calcined at temperatures ranging from 300 to 500°C to obtain ZnO nanoparticles [31–36].

2.2. Preparation of ZnO/TiO_2 nanocomposites using the chemical precipitation method

ZnO/TiO_2 nanocomposites were synthesized using the chemical co-precipitation method. A 0.1 M zinc chloride ($ZnCl_2$) solution (100 mL) was prepared in a glass beaker and stirred at room temperature at a rate of 300–600 rpm. Subsequently, a 0.1 M titanium chloride solution was added dropwise under continuous stirring. After thorough mixing, a 0.2 M sodium hydroxide (NaOH) solution was gradually introduced to adjust the pH of the reaction mixture to approximately 8–10.

The resulting suspension was continuously stirred for 30–60 min to ensure homogeneous precipitation. The precipitate was then collected and repeatedly washed with deionized water followed by ethanol to remove residual ions and impurities. Afterward, the product was dried in an oven at 60–100°C and subsequently calcined in an electric furnace at 400–550°C for 2 h to obtain the ZnO/TiO_2 nanocomposite. Co-precipitation, which involves the simultaneous precipitation of two or more components from the same solution, is a widely used method for the synthesis of binary, ternary, and mixed oxide compounds with controlled composition and crystalline structure [37].

2.3. Preparation of ZnO/NiO nanocomposites using the chemical precipitation method

The ZnO/NiO nanocomposite was synthesized via the chemical co-precipitation method by mixing 100 mL of 0.1 M $ZnCl_2$ solution with 100 mL of 0.1 M $NiCl_2 \cdot 6H_2O$ solution under continuous stirring. An anti-caking agent, PVP, was added during the mixing process to improve the homogeneity of the resulting precipitate. Subsequently, a 0.2 M NaOH solution was added dropwise while continuously monitoring the pH of the reaction mixture until a pH value of 9–11 was reached, leading to the precipitation of the corresponding metal hydroxides. Stirring was maintained for an additional period to ensure complete precipitation and uniform mixing. The precipitate was collected by centrifugation and repeatedly washed with deionized water, followed by ethanol to remove residual chloride ions and other impurities. The obtained product was then dried in an oven at 80–100°C and subsequently calcined in an electric furnace at 400–600°C for 2 h to obtain the ZnO/NiO nanocomposite. Co-precipitation is a widely employed technique for the synthesis of mixed-metal oxide nanocomposites, enabling the homogeneous incorporation of NiO and ZnO within the composite structure and thereby enhancing its functional properties [38].

2.4. Preparation of the Anode Electrodes

The photoelectrodes were fabricated using the synthesized nanomaterials prepared by the precipitation method, as described previously. A small amount of the prepared nanomaterial was mixed with deionized water (DIW) and acetic acid to form a homogeneous paste. The resulting paste was then uniformly coated onto fluorine-doped tin oxide (FTO) glass substrates, leaving the edges uncovered to prevent electrical short-circuiting. The coated substrates were dried in an oven at 40–50°C until complete solvent removal was achieved. Subsequently, the prepared photoelectrodes were immersed in the red dye solution (Dye 1) and kept in a dark environment for 24 h to allow sufficient dye adsorption onto the nanomaterial surface. After sensitization, the photoelectrodes were removed from the dye solution and dried in the dark to obtain the dye-sensitized anodes. The same procedure was followed for the fabrication of photoelectrodes based on the synthesized ZnO/TiO_2 and ZnO/NiO nanocomposites using the selected dye sensitizers. For cathode preparation, a thin layer of polished carbon was uniformly deposited onto the conductive side of an FTO glass substrate while leaving the edges uncovered. The resulting carbon-coated substrate was then used as the counter electrode (cathode) in the DSSC assembly. To ensure experimental consistency and reproducibility, the key fabrication parameters were carefully controlled and optimized. The thickness of the photoanode films was determined to be approximately 14 μm using the gravimetric method. The effective active area of the fabricated DSSCs was 1.6 cm^2, as defined by the coating area on the FTO substrate. To promote crystallization and improve film adhesion, the deposited photoanode films were thermally annealed at 400 °C for 30 min. For sensitization, an E133 dye solution with a concentration of 0.05 mM was prepared. The natural red cabbage

dye was extracted by blending 100 g of red cabbage with 50 mL of ethanol using an electric blender. The resulting mixture was filtered to remove solid residues and subsequently stored in a dark environment until use as a natural dye sensitizer. The electrolyte solution consisted of 0.1 M potassium iodide (KI) and 0.1 M iodine (I_2) dissolved in an appropriate solvent. Fluorine-doped tin oxide (FTO) glass with a surface resistivity of 15 Ω/m^2 was used as the conductive substrate. To prevent electrolyte leakage and ensure proper cell assembly, the fabricated DSSCs were sealed using double-sided thermal adhesive tape.

3. Results and Discussion

X-ray diffraction (XRD) analysis was performed to characterize the crystalline structure of the prepared ZnO nanoparticles. The diffraction pattern exhibited characteristic peaks at 2θ values of 31.737°, 34.379°, 36.215°, 47.484°, 56.536°, 62.777°, 66.304°, and 67.868°, corresponding to the crystallographic planes (100), (002), (101), (102), (110), (103), (200), and (112), respectively. These diffraction peaks are in good agreement with the standard data reported in the Joint Committee on Powder Diffraction Standards (JCPDS) card No. 01-076-0704, confirming the formation of the hexagonal wurtzite phase of ZnO, as shown in Figure 1 [39]. The observed diffraction peaks were sharp and intense, indicating a high degree of crystallinity and phase purity. No additional peaks associated with impurity phases were detected, confirming the successful synthesis of single-phase ZnO nanoparticles. The average crystallite size (D) was estimated using the Debye–Scherrer equation based on the full width at half maximum (FWHM) of the most intense diffraction peak [40]. The obtained results confirmed the formation of ZnO nanoparticles with a hexagonal nanostructure.

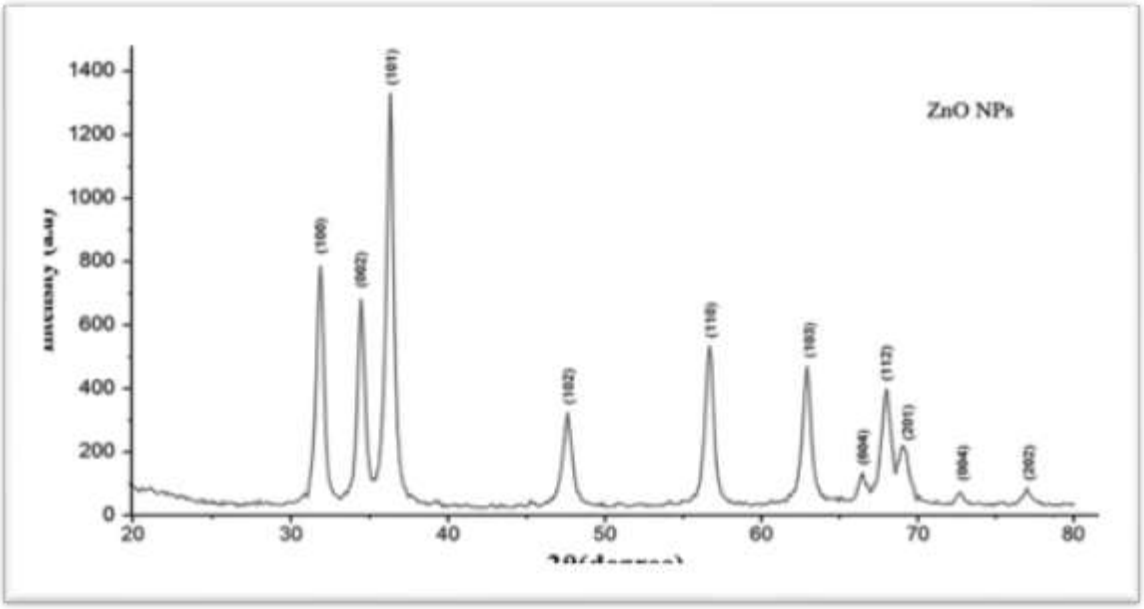


Figure 1. shows the X-ray diffraction (XRD) pattern of the ZnO nanostructures.

X-ray diffraction (XRD) analysis was employed to investigate the crystalline structure and phase composition of the synthesized ZnO/TiO_2 nanocomposites, as illustrated in Fig. 2. The diffraction patterns confirmed the polycrystalline nature of both ZnO and TiO_2 phases within the nanocomposite structure. The results revealed that the nanocomposite consists of tetragonal rutile TiO_2 (JCPDS card No. 01-087-0920) and hexagonal wurtzite ZnO (JCPDS card No. 01-067-0704) phases [41,42]. The characteristic diffraction peaks observed at approximately 2θ = 27.4°, 36.1°, 41.2°, and 54.3° were indexed to the (110), (101), (111), and (211) crystallographic planes of tetragonal rutile TiO_2, respectively [43,44]. These findings confirm the successful formation of the rutile TiO_2 phase within the ZnO/TiO_2 nanocomposite. The absence of additional impurity peaks indicates the successful synthesis of highly crystalline TiO_2 nanoparticles with high phase purity. Furthermore, the observed diffraction peaks of ZnO were indexed to the hexagonal wurtzite crystal structure.

The characteristic ZnO peaks located at approximately 2θ = 31.7°, 34.4°, 36.2°, 47.5°, and 56.5° were assigned to the (100), (002), (101), (102), and (110) crystallographic planes, respectively. In the ZnO/TiO_2 nanocomposite, diffraction peaks corresponding to both ZnO and TiO_2 phases were clearly observed, confirming the successful formation of the composite structure. The coexistence of these diffraction peaks indicates the simultaneous growth of hexagonal ZnO and tetragonal rutile TiO_2 phases without the formation of secondary impurity phases, demonstrating the high crystallinity and phase purity of the synthesized nanocomposite. The strong agreement between the observed diffraction peaks and the standard JCPDS data further confirms the high crystallinity and phase purity of the synthesized nanocomposite materials.

The average crystallite size (D) was estimated using the Debye–Scherrer equation [45]:

$$D = \frac{K\lambda}{\beta \cos\theta}$$

where D is the crystallite size, K is the shape factor (0.9), λ is the X-ray wavelength, β is the full width at half maximum (FWHM), and θ is the Bragg diffraction angle.

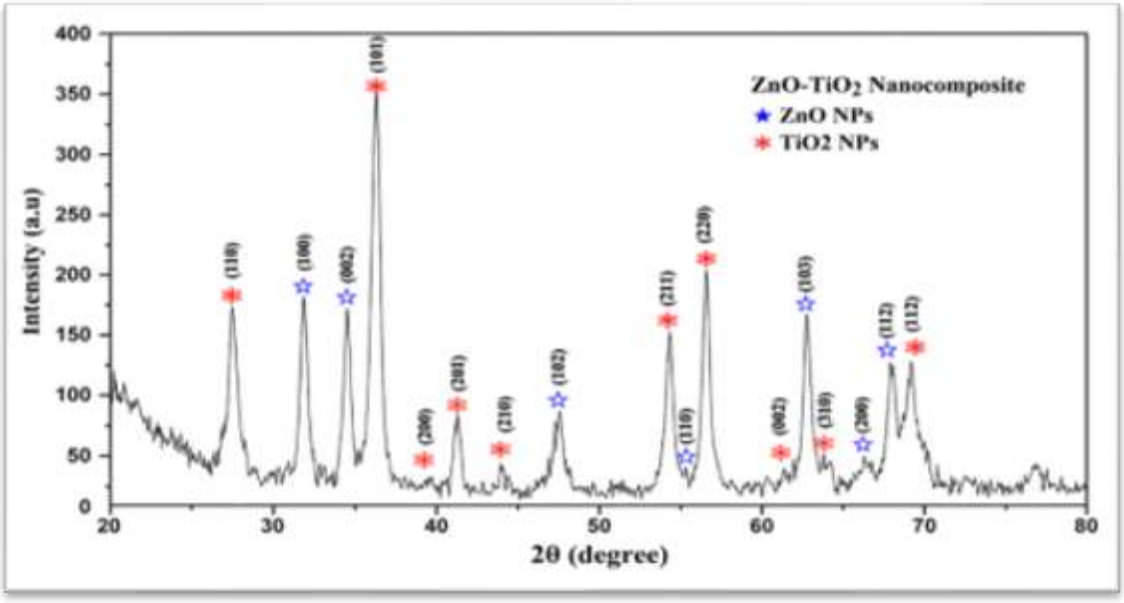


Figure 2. shows the X-ray diffraction (XRD) pattern of the synthesized ZnO/TiO_2 nanocomposite.

X-ray diffraction (XRD) analysis was employed to investigate the crystalline structure and phase composition of the synthesized ZnO/NiO nanocomposite, as shown in Figure 3. The diffraction pattern revealed the presence of characteristic peaks corresponding to both ZnO and NiO phases, confirming the polycrystalline nature of the nanocomposite. The results indicate that the composite consists of hexagonal wurtzite ZnO (JCPDS card No. 00-036-1451) and cubic NiO (JCPDS card No. 01-078-0643) phases. The observed diffraction peaks are in good agreement with the standard JCPDS reference data, confirming the successful formation of the ZnO/NiO nanocomposite without detectable impurity phases. The average crystallite size, estimated using the Debye–Scherrer equation, was found to range from 16.55 to 39.56 nm.

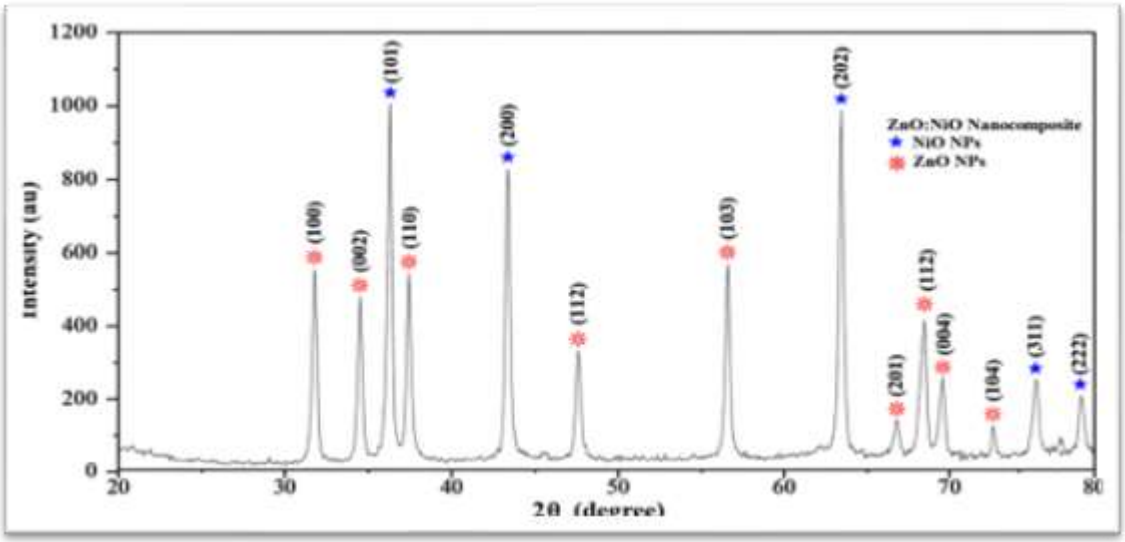


Figure 3. shows the X-ray diffraction (XRD) pattern of the synthesized ZnO/NiO nanocomposite

3.1. Analysis of Field Emission Scanning Electron Microscopy (FE-SEM)

Field emission scanning electron microscopy (FE-SEM) pictures of the produced zinc oxide (ZnO) nanoparticles and ZnO/TiO_2 and ZnO/NiO nanocomposites are displayed in Figures 4, 5, and 6. The average diameter is 15.67 nm, and Figure 4 provides additional proof that the zinc oxide (ZnO) is developing as an interconnecting network of nanoparticles. Field emission scanning electron microscopy (FESEM) images captured at various magnifications were used to determine the microstructure and texture of the produced samples. FESEM pictures of the ZnO/TiO_2 composites at various magnifications are displayed in Figure 5. These pictures demonstrate that the composite nanoparticles are made up of highly porous fibrous microstructures with rough, uneven surfaces and sizes between 16.06 and 19.25 nm. Field-emission scanning electron microscopy (FE-SEM) pictures of the ZnO/NiO composites at different magnifications are displayed in Figure 6, with a mean diameter of 23.19 nm. The produced sample's surface area thus increases dramatically, drastically enhancing the adsorption process and catalytic efficacy.

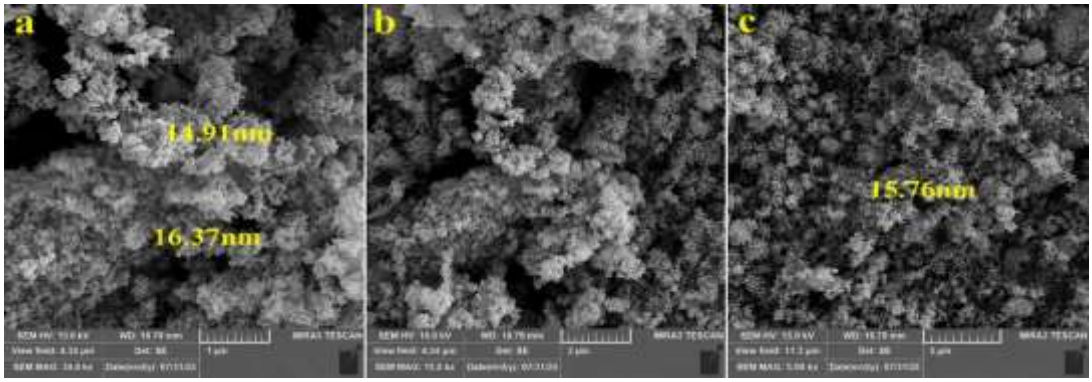


Figure 4. FE-SEM image of ZnO NPs a- 1µm b- 2 µm c- 5 µm.

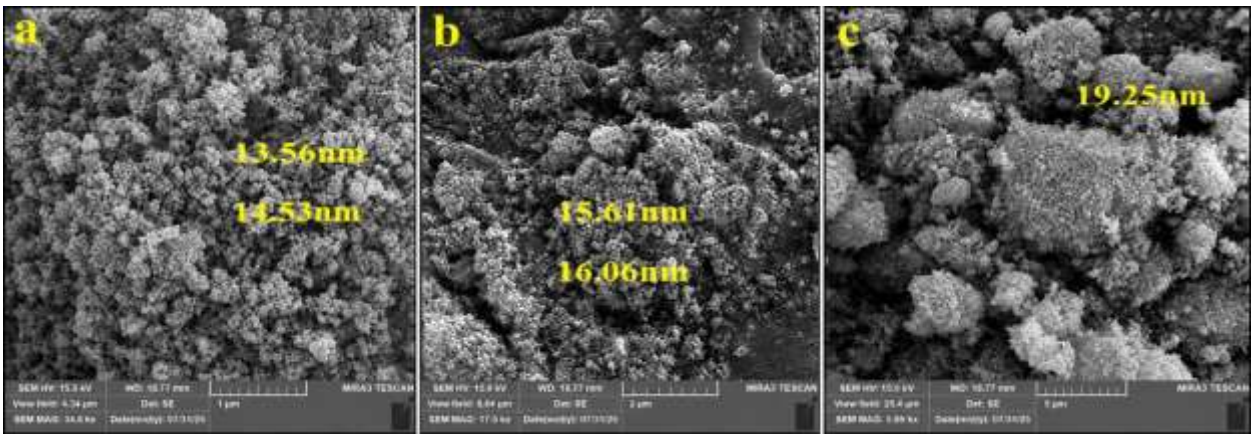


Figure 5. FE-SEM image of ZnO/TiO_2 nanocomposite a- 1µm b- 2µm c- 5 µm.

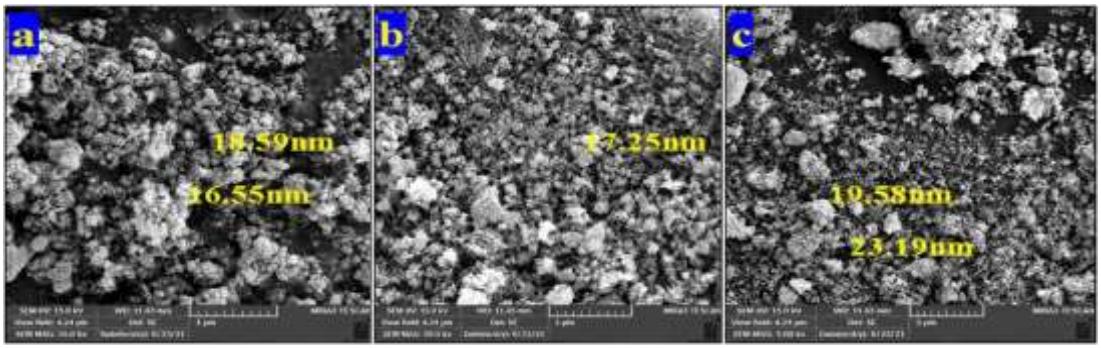


Figure 6. FE-SEM image of ZnO/NiO nanocomposite a- 1µm b- 2µm c- 5 µm.

3.2. Analysis of Transmission Electron Microscopy (TEM)

The produced nanoparticles and composite nanomaterials were assessed using transmission electron microscopy (TEM) analysis. ZnO nanoparticles with diameters ranging from 16 to 31.32 nm have a spherical form, as seen in Figure 7. ZnO/TiO_2 nanoparticles, which range in size from 52 to 55.5 nm, are depicted in Figure 8. ZnO/NiO nanoparticles with sizes and morphologies ranging from 62.48 to 68.99 nm are depicted in Figure 9.

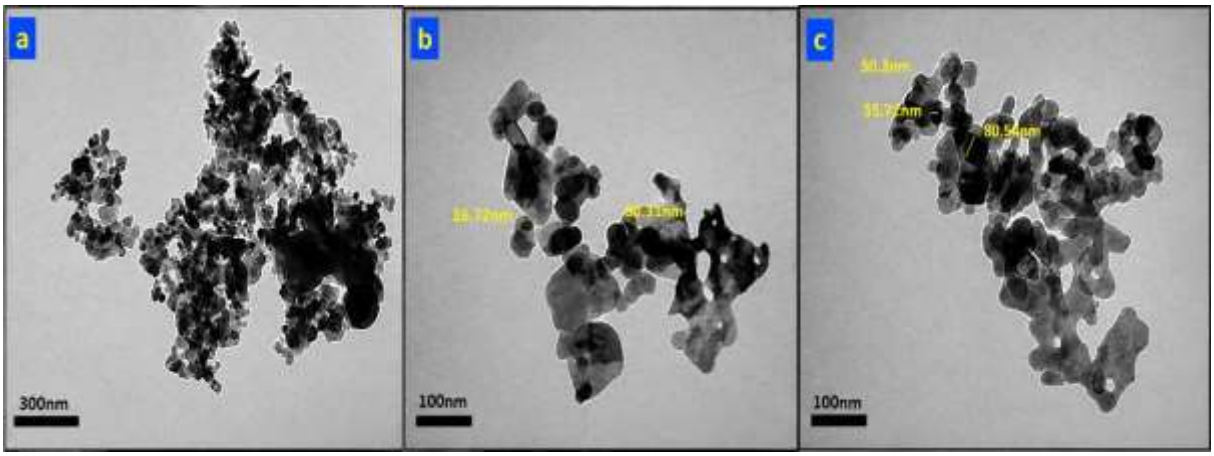


Figure 7. TEM image of ZnO NPs a-300 nm b-100 nm c- 100nm.

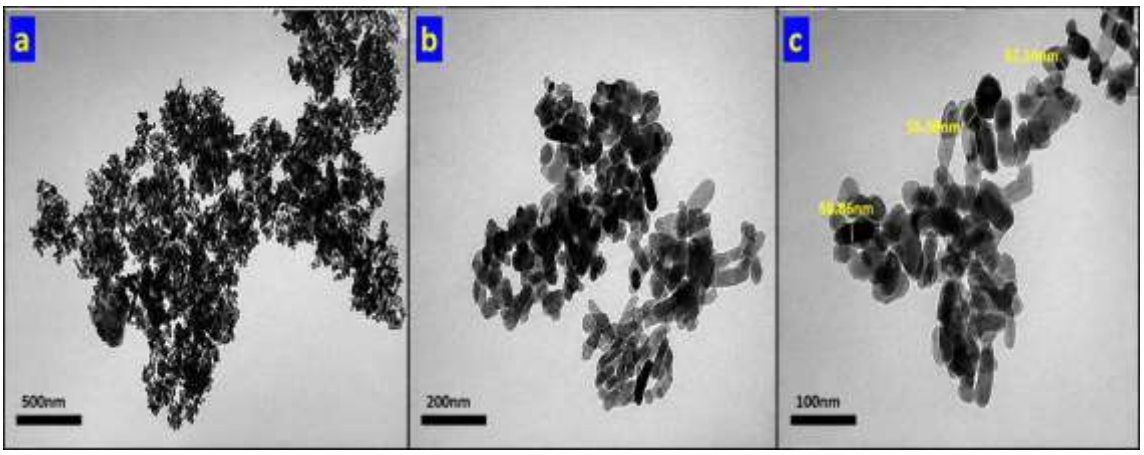


Figure 8. TEM image of ZnO/TiO2 nanocomposite a-500 nm b-200 nm c- 100nm.

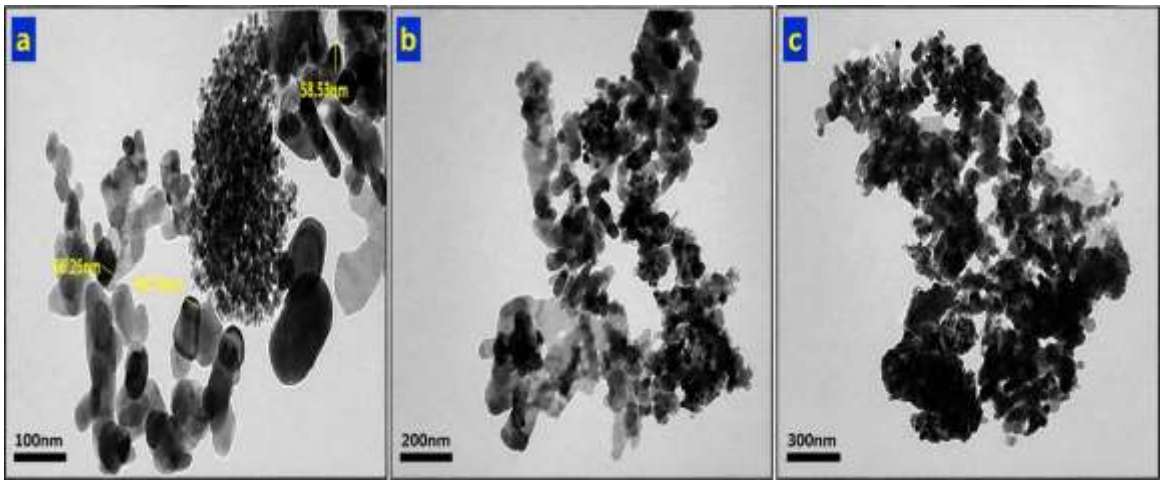


Figure 9: TEM image of ZnO/NiO nanocomposite a-100 nm b-200 nm c- 300nm.

3.3. Brunauer-Emmett-Teller Specific Surface Area (BET) Analysis

By adsorbing nitrogen gas at -196°C on the surface, BET analysis is performed to determine the surface area of ZnO, ZnO/TiO_2, and ZnO/NiO. Table 1 presents the results. The surface area and total pore size of all the produced nanoparticles and compounds are displayed in the table below, since a larger surface area results in more efficient solar cell operation and photocatalytic degradation.

Table 1. The distinctive surface of the BET method's nanoparticles and nanocomposites.

Compound	Surface area m^2 /g	Total pore volume (P/Po=0.95) cm^3 /g	Mean pore diameter nm
ZnO	26.6293	0.065368	9.81899
ZnO / TiO_2	41.3756	0.094626	9.14797
ZnO / NiO	35.8927	0.089693	8.33141

3.4. Fourier Transform Infrared Spectroscopy Analysis (FT-IR)

Fourier transform infrared (FTIR) spectroscopy was employed to identify the functional groups present in the synthesized ZnO nanoparticles and nanocomposites. The FTIR spectrum of ZnO nanoparticles (ZnO NPs), recorded in the range of 400–4000 cm^{-1}, is presented in Figure 10. A distinct absorption band observed in the 450–500 cm^{-1} region is attributed to the stretching vibrations of Zn–O bonds, confirming the formation of crystalline ZnO. The broad absorption band centered around 3400 cm^{-1} is assigned to O–H stretching vibrations, indicating the presence of adsorbed water molecules and surface hydroxyl groups on the ZnO nanoparticles. The absorption bands observed in the 2850–2920 cm^{-1} region correspond to C–H stretching

vibrations, which may arise from residual organic species such as solvents or stabilizing agents used during the synthesis process. Furthermore, the bands located in the 1650–1570 cm^{-1} and around 1420 cm^{-1} regions can be attributed to H–O–H bending vibrations of adsorbed water molecules and/or C=O and C–O vibrations associated with carbonate species present on the particle surface. The presence of these surface functional groups is commonly observed in ZnO nanoparticles and may influence their surface properties and chemical reactivity. Overall, the FTIR results confirm the successful formation of crystalline ZnO nanoparticles, together with the presence of adsorbed moisture and minor carbonate or organic residues originating from the synthesis process or ambient environmental exposure.

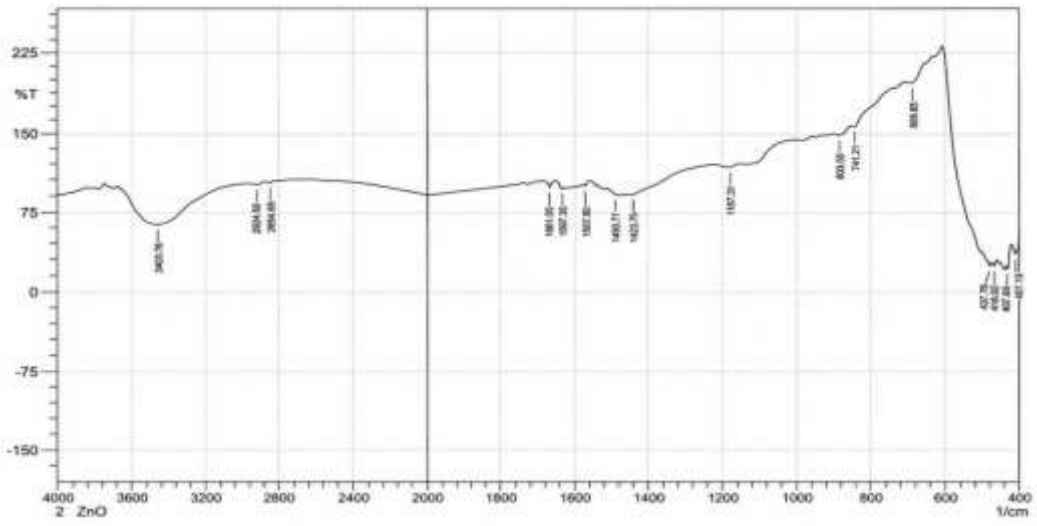


Figure10. ZnO nanoparticles' FTIR spectrum.

The Fourier transform infrared (FTIR) spectrum of the ZnO/TiO_2 nanocomposite is presented in Figure 11. The spectrum exhibits several characteristic absorption bands that provide information about the chemical composition and surface functional groups of the synthesized nanocomposite. The absorption bands observed in the range of 441.70–686.66 cm^{-1} are attributed to the metal–oxygen vibrations of Zn–O, Ti–O, and Zn–O–Ti bonds, confirming the presence of both ZnO and TiO_2 phases and indicating the successful formation of the ZnO/TiO_2 nanocomposite. A broad absorption band centered at 3425.58 cm^{-1} is assigned to O–H stretching vibrations, which are commonly associated with surface hydroxyl groups and adsorbed water molecules on metal oxide nanoparticles. The absorption bands located at 2929.87 and 2960.73 cm^{-1} correspond to C–H stretching vibrations, suggesting the presence of trace organic residues, such as ethanol or stabilizing agents used during the synthesis process. Furthermore, the absorption bands observed at 1629.85 and 1676.14 cm^{-1} are attributed to the H–O–H bending vibrations of adsorbed water molecules. These results confirm the successful formation of the ZnO/TiO_2 nanocomposite and the presence of surface hydroxyl groups and adsorbed moisture, which may influence the surface properties of the material.

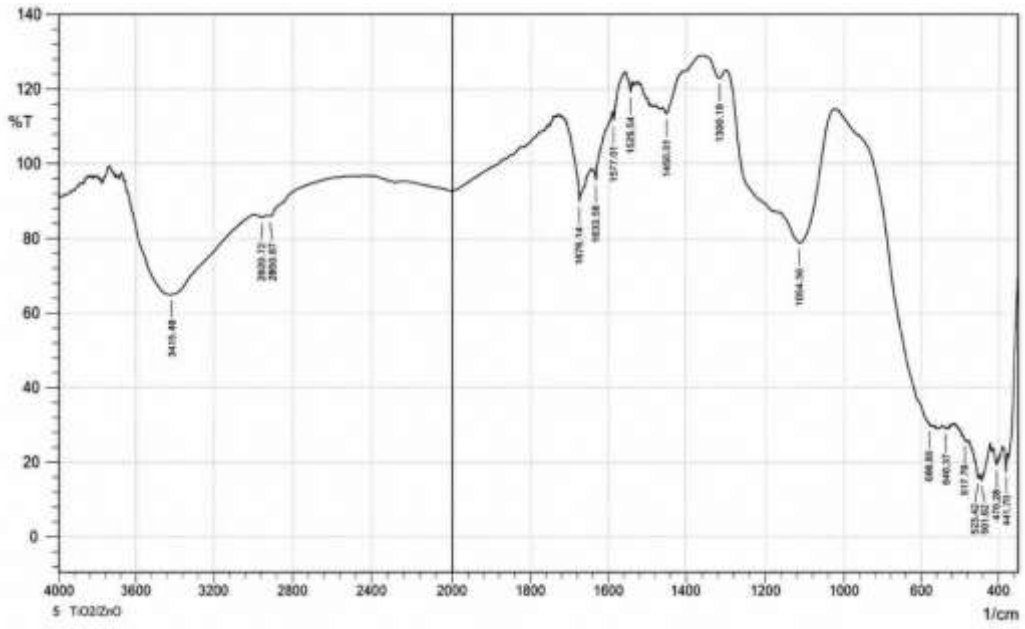


Figure 11. ZnO/TiO2 nanocomposite's FTIR spectra.

Figure 12 presents the Fourier transform infrared (FTIR) spectrum of the ZnO/NiO nanocomposite. The absorption bands observed in the range of 410.84–600 cm^{-1} are attributed to the characteristic metal–oxygen vibrations of Zn–O and Ni–O bonds, confirming the successful formation of the ZnO/NiO nanocomposite and the presence of both metal oxide phases. A broad and intense absorption band centered at 3454.51 cm^{-1} is assigned to O–H stretching vibrations, which are commonly associated with surface hydroxyl groups and adsorbed water molecules on the nanocomposite surface. The absorption bands located at 1633.71 and 1666.50 cm^{-1} are attributed to the H–O–H bending vibrations of adsorbed water molecules and/or surface hydroxyl groups. Furthermore, the bands observed at 1438.90 and 1489.05 cm^{-1} can be assigned to C–O and C–O–H vibrations associated with carbonate species formed through the interaction of the metal oxides with atmospheric CO_2. The presence of these surface functional groups is commonly observed in metal oxide nanomaterials and may influence their surface chemistry and adsorption behavior. Overall, the FTIR results confirm the successful synthesis of the ZnO/NiO nanocomposite and the presence of characteristic metal–oxygen bonds, surface hydroxyl groups, adsorbed moisture, and carbonate species.

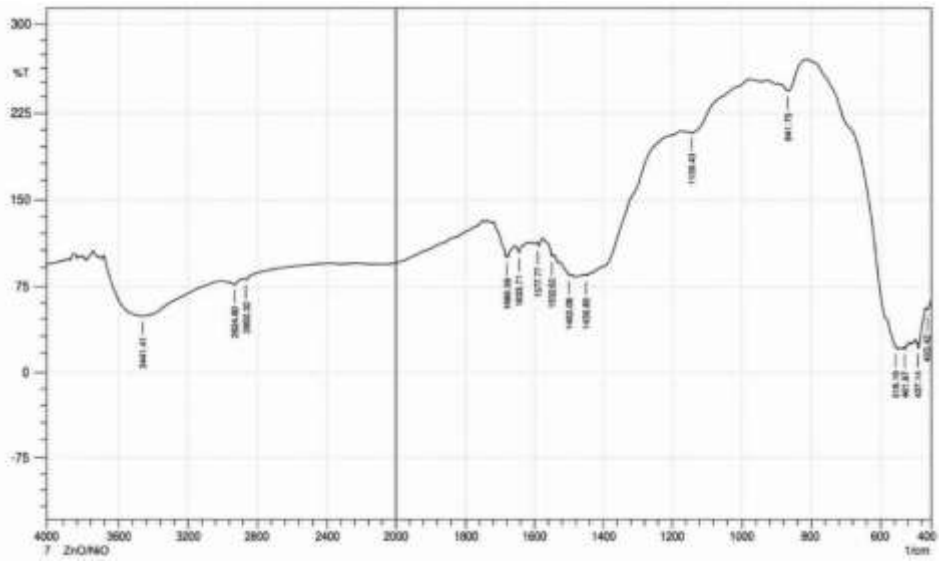


Figure 12. ZnO/NiO nanocomposite's FTIR spectrum.

3.5. Optical Properties

The optical properties of the synthesized nanomaterials, namely ZnO, ZnO/TiO_2, and ZnO/NiO, were investigated using UV–Vis absorption spectroscopy, and the corresponding spectra are presented in Figures 13–15, respectively. Figure 13 illustrates the absorbance spectrum as a function of wavelength, along with the Tauc plot ((αhν)2) versus (hν), for ZnO nanoparticles synthesized via the precipitation method. The optical band gap energy was estimated from the Tauc plot and found to be 3.309 eV. This value is in good agreement with those reported in previous studies for ZnO, which typically range from 3.10 to 3.37 eV [46]. The obtained result confirms the successful formation of ZnO nanoparticles with optical properties characteristic of semiconductor metal oxides.

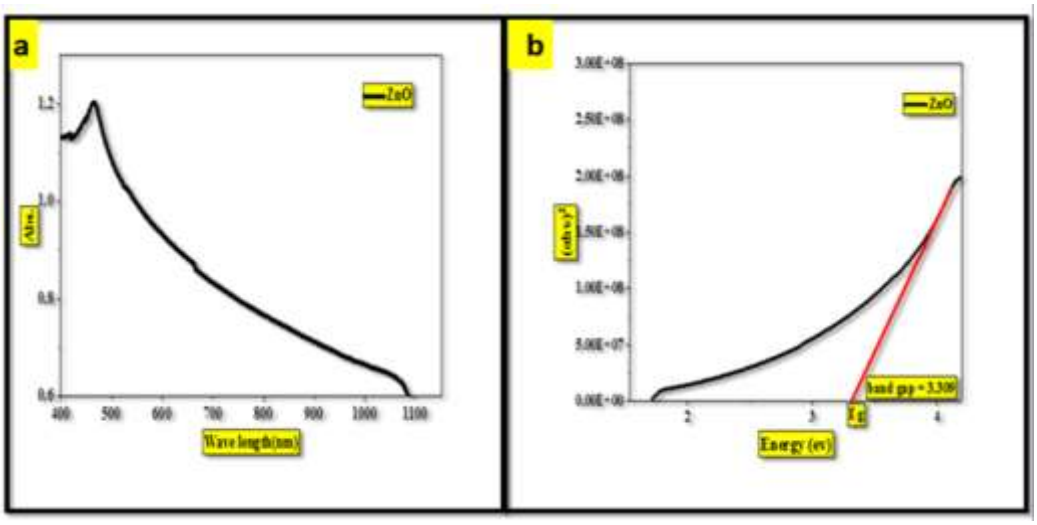


Figure 13. The absorbance spectrum b) ZnO's Eg optical energy band gap.

Figure 14 presents the UV–Vis absorption spectrum as a function of wavelength, together with the Tauc plot of ((αhν)2) versus (hν), for the ZnO/TiO_2 nanocomposite synthesized via the precipitation method. The optical band gap energy was estimated from the Tauc plot and found to be 3.1 eV. This value is consistent with those reported in the literature for similar ZnO/TiO_2 nanocomposites, which typically range from approximately 3.1 to 3.3 eV [47]. The relatively narrow band gap facilitates light absorption and promotes efficient charge generation and transfer processes. These characteristics are advantageous for dye-sensitized solar cell (DSSC) applications, as they can enhance photoinduced electron transport and improve the overall photovoltaic performance of the device.

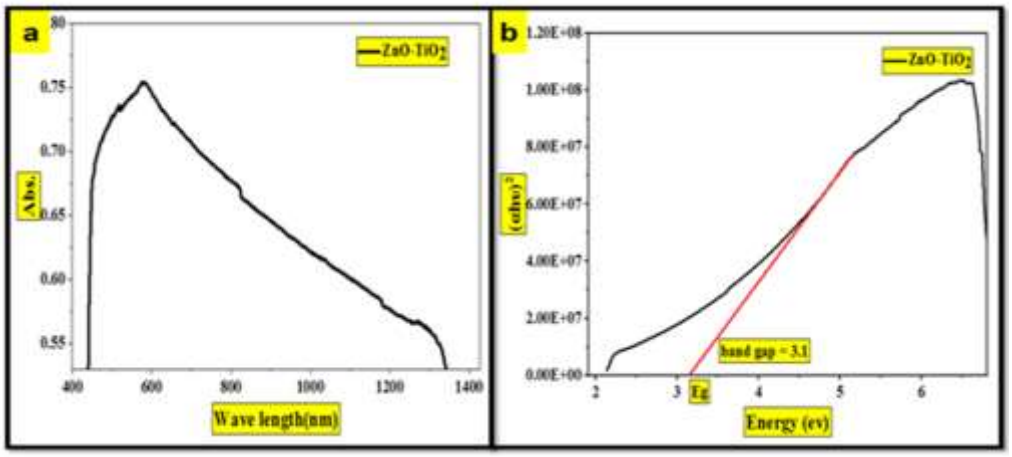


Figure 14. The absorbance spectrum b) The ZnO/TiO_2 nanocomposite's Eg optical energy band gap.

Figure 15 presents the UV–Vis absorption spectrum as a function of wavelength, together with the Tauc plot of $((\alpha h\nu)^2)$ versus $(h\nu)$, for the ZnO/NiO nanocomposite synthesized via the precipitation method. The optical band gap energy was estimated from the Tauc plot and found to be 3.018 eV. This value is in good agreement with those reported in the literature for ZnO/NiO nanocomposites and related metal oxide systems, which typically range from approximately 2.6 to 3.7 eV [48]. The reduced band gap facilitates enhanced light absorption and promotes efficient charge separation and transfer processes. These properties are beneficial for dye-sensitized solar cell (DSSC) applications, where improved photoinduced electron transport can contribute to enhanced photovoltaic performance.

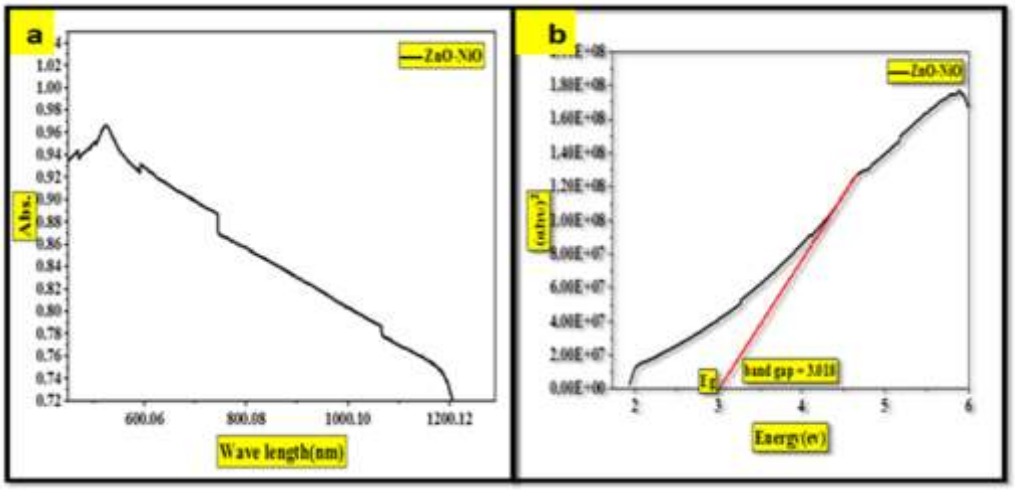


Figure 15. The absorbance spectrum and the ZnO/NiO nanocomposite's Eg optical energy band gap.

Table 2. shows the synthesized nanoparticles' and nanocomposites' energy range band gap.

Compound	ZnO	ZnO/TiO_2	ZnO/NiO
Eg	3.3 eV	3.1 eV	3.0 eV

The structural and morphological characteristics of the synthesized nanostructured oxides are closely related to the photovoltaic performance of the fabricated DSSCs. SEM analysis revealed that the synthesized nanocomposites possess porous and relatively homogeneous surface morphologies, providing a large active surface area for dye adsorption and facilitating efficient electrolyte diffusion throughout the photoanode layer. Such porous structures are known to enhance light-harvesting capability and improve charge transport processes in DSSCs [49,50]. The increased surface area promotes higher dye loading, while the interconnected porous network facilitates electron transport and improves contact between the photoanode and the electrolyte. These features contribute to enhanced photoelectrochemical activity and can lead to improved photovoltaic performance of the DSSCs. Furthermore, X-ray diffraction (XRD) analysis confirmed the crystalline nature of ZnO, TiO_2, NiO, and their corresponding nanocomposites. The high crystallinity and phase purity of the synthesized materials may contribute to reducing structural defects and suppressing electron–hole recombination, thereby facilitating charge transport and enhancing the photovoltaic performance of the DSSCs[50,5]. In addition, the optical properties and band gap energies of the synthesized nanocomposites are closely related to the observed improvement in DSSC performance. Appropriate band gap values can promote efficient light absorption and photoinduced charge generation, leading to enhanced electron injection and charge-transfer processes within the photoanode. Consequently, these characteristics contribute to improved photovoltaic efficiency of the fabricated solar cells. Under solar irradiation, the observed reduction in band gap energy of the synthesized nanocomposites may enhance visible-light absorption and facilitate photoinduced electron excitation [51,52]. Similar behavior has been reported in previous studies, where ZnO/TiO_2 and ZnO/NiO nanocomposites exhibited improved charge separation efficiency and enhanced dye

adsorption capability as a result of favorable interfacial interactions between the semiconductor oxides [51,53]. Furthermore, the incorporation of TiO_2 and NiO into the ZnO matrix may promote interfacial charge transfer and reduce charge recombination losses, leading to increased photocurrent density and improved power conversion efficiency [50,52]. Overall, the relationship between morphology, crystal structure, optical properties, and photovoltaic performance suggests that high crystallinity, porous surface morphology, and enhanced optical absorption act synergistically to improve the efficiency of dye-sensitized solar cells (DSSCs). These combined characteristics contribute to more efficient light harvesting, improved charge transport, and reduced electron–hole recombination, thereby enhancing the overall photovoltaic performance of the fabricated devices. These findings are consistent with previous studies on semiconductor nanocomposites for solar energy applications [50–53]. The porous nanostructures provide a large surface area for dye adsorption and facilitate efficient electron transport pathways within the photoanode layer, thereby enhancing the photovoltaic performance of DSSCs [54]. Furthermore, the high crystallinity and reduced structural defects of the synthesized nanocomposites may suppress charge recombination processes and improve electron mobility, contributing to more efficient charge collection [56]. Under solar irradiation, the observed reduction in band gap energy can enhance visible-light absorption and promote increased photocurrent generation [54,55]. In addition, previous studies have reported that ZnO/TiO_2 nanocomposites exhibit enhanced interfacial charge transfer and prolonged electron lifetime due to the favorable band alignment between the constituent semiconductor materials [54]. These characteristics facilitate efficient charge separation and reduce recombination losses, ultimately leading to improved DSSC performance.

3.6. Production of Dye-Sensitive Solar Cells

To produce dye-sensitive solar cells, zinc oxide (ZnO), zinc oxide/titanium dioxide (ZnO/TiO_2) nanoparticles, and zinc oxide/nickel oxide (ZnO/NiO) nanoparticles were synthesized. These particles were used as photoconductors with two dyes—a blue dye (fluorescent blue FCF-E133) and a red dye (cabbage red)—as absorbers. Figures 16 to 21 show the current-voltage curves and other characteristics of the dye-sensitive solar cells made from the nanoparticles and natural dyes. Compared to the red dye, the blue dye increases the energy conversion efficiency (η) of the dye-sensitive solar cells, as shown in Tables 3 and 4. The absorption spectra indicate that the red dye exhibits lower absorption intensity compared to the blue dye (Brilliant Blue FCF), suggesting a lower molar absorption coefficient and, consequently, lower photocurrent generation (Jsc). Furthermore, the molecular structure of the anthocyanin weakens its bonding to the zinc oxide surface, resulting in less efficient electron injection and increased recombination losses. Therefore, the improved performance of the blue dye is primarily attributed to its stronger absorption in the visible region and its superior adsorption capacity on the semiconductor surface. Due to the increased concentration of natural pigment impurities, the current of DSSC cells made with natural red pigment is lower than the current of DSSC cells made with blue pigment [57].

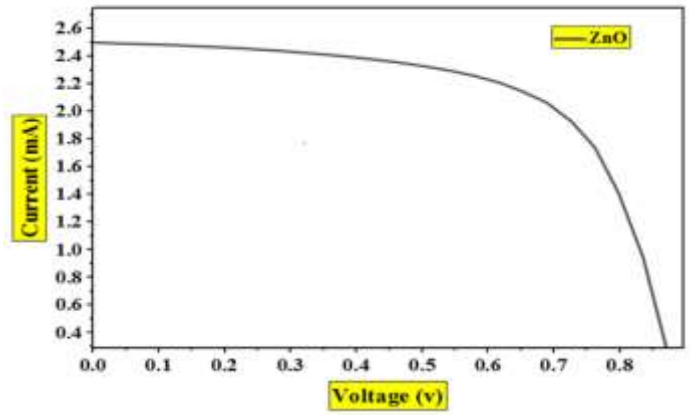


Figure 16. I–V characteristics of the ZnO DSSC sensitized with Brilliant Blue FCF (E133).

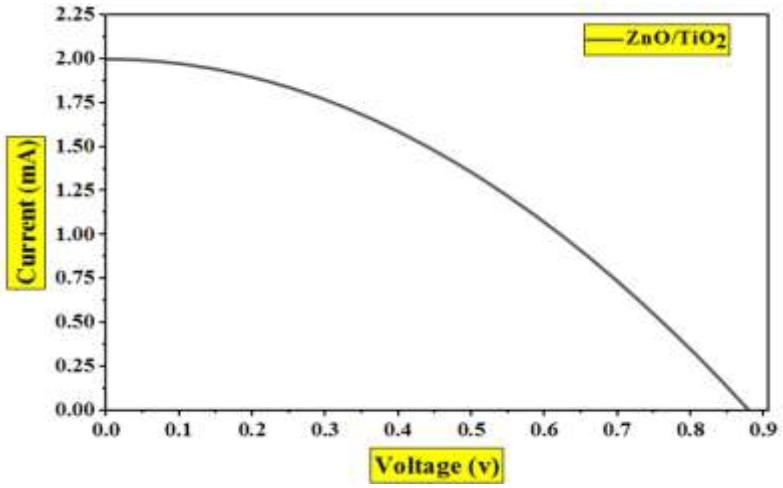


Figure 17. I–V characteristics of the ZnO/TiO_2 DSSC sensitized with Brilliant Blue FCF (E133).

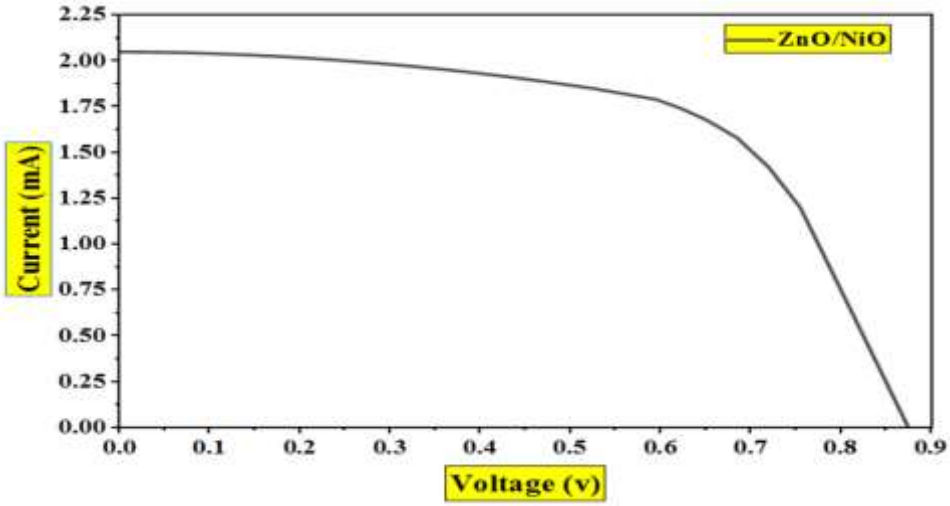


Figure 18. I–V characteristics of the ZnO/NiO DSSC sensitized with Brilliant Blue FCF (E133).

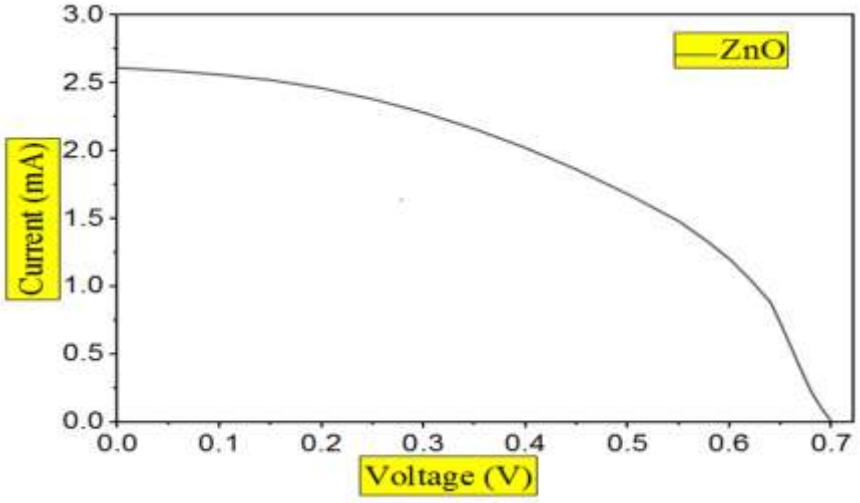


Figure 19. I–V characteristics of the ZnO DSSC sensitized with red cabbage extract.

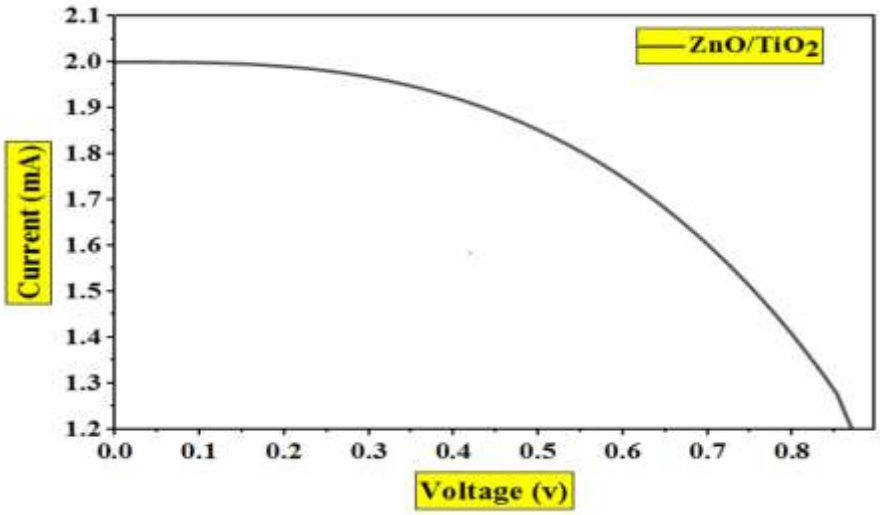


Figure 20. I–V characteristics of the ZnO/TiO_2 DSSC sensitized with red cabbage extract.

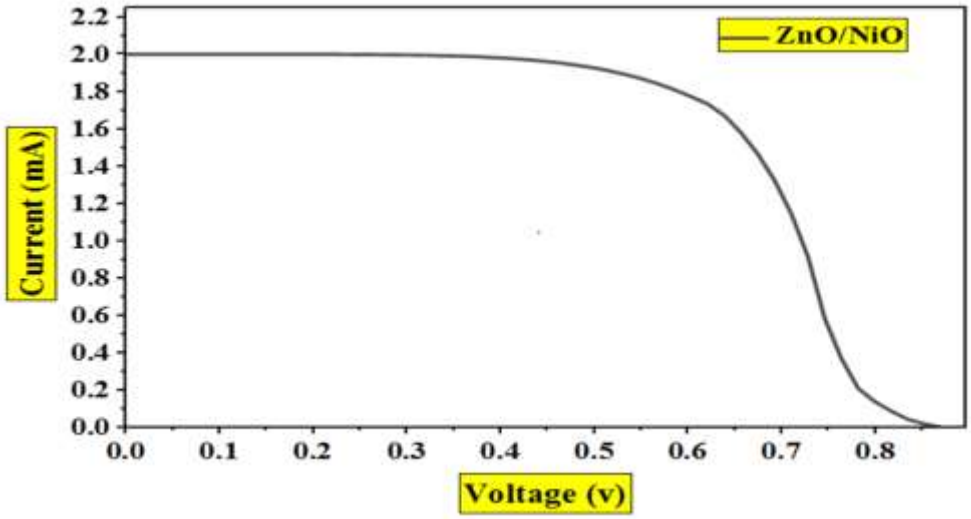


Figure 21. I–V characteristics of the ZnO/NiO DSSC sensitized with red cabbage extract.

Table 3. Photo-electrochemical parameters of DSSCs (A = 1.6 cm² blue dye) with a light intensity of 22.53 mW/cm².

Catalyst	ISC (mA)	Voc (V)	Imax (mA)	Vmax (V)	Pmax (mW)	FF	η %
ZnO	2.5	0.87	1.8408	0.7569	1.3933	0.6406	3.865
ZnO/TiO_2	2.0	0.88	1.8347	0.6233	1.1436	0.6498	3.172
ZnO/NiO	2.05	0.875	1.740	0.623	1.083	0.603	3.050

Table 4. Photo-electrochemical parameters of DSSCs (A = 1.6 cm² red dye) with a light intensity of 22.53 mW/cm².

Catalyst	ISC (mA)	Voc (V)	Imax (mA)	Vmax (V)	Pmax (mW)	FF	η %
ZnO	2.61	0. 7	1. 48	0.52	0.77	0.65	3.3
ZnO/TiO_2	2.0	0.87	1.4641	0.7612	1.1145	0.6405	3.090
ZnO/NiO	2.0	0.87	1.7322	0.6214	1.0764	0.6186	2.986

The use of carbon as the counter electrode on the rear surface of the FTO-based solar cell, along with the relatively low light intensity of the illumination source (22.53 mW/cm²), contributes to the comparatively low performance of the fabricated DSSCs. In addition, an iodine/iodide (I^-/I_3^-) electrolyte solution was prepared to provide ionic conductivity within the device. The photovoltaic performance of the dye-sensitized solar cells (DSSCs) was evaluated using a Keithley 2400 source meter, as shown in Figure 22. Basic current–voltage (I–V) measurements provide most of the essential photovoltaic parameters of the solar cell. The current and voltage characteristics under illumination and forward bias conditions are presented in Table 1. The short-circuit current (Isc) is defined as the current flowing through the solar cell when the voltage is zero. The open-circuit voltage (Voc) is defined as the voltage across the solar cell when the current is zero, representing the maximum potential difference generated by the device [58]. The maximum power point (Pmax) corresponds to the operating condition at which the solar cell delivers its highest output power, where the corresponding voltage and current are denoted as Vmax and Imax, respectively. Two key parameters are commonly used to evaluate solar cell performance: the fill factor (FF) and the power conversion efficiency (η) [59]. The fill factor is defined as the ratio of the maximum power (Pmax) to the product of open-circuit voltage (Voc) and short-circuit current (Isc). The conversion efficiency is defined by Equations (1–4) as the ratio of the maximum electrical power output (Pmax) to the incident light power (E × Ac), where E is the light intensity and Ac is the active area of the solar cell [60]. The relatively low fill factor (FF ≈ 0.6) may be associated with increased internal resistance and charge transfer resistance at the carbon-based counter electrode, leading to enhanced recombination losses at the electrode/electrolyte interface.

$$FF = \frac{Pmax}{Voc \times Isc} \quad (1)$$

$$\eta = \frac{Voc \times Isc \times FF}{E} \quad (2)$$

$$FF = \frac{Vmax \times Imax}{Voc \times Isc} \quad (3)$$

$$\%\eta = \frac{Voc \times Isc \times FF}{Pin} \quad (4)$$

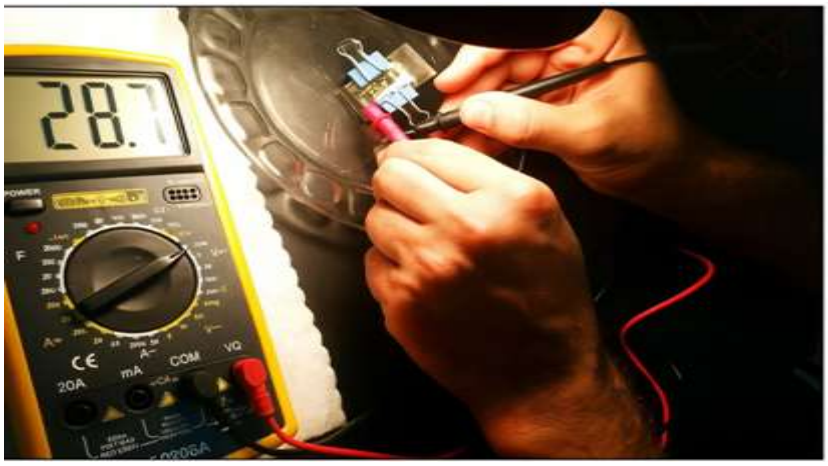


Figure 22. shows the measurement of solar cell voltage under the influence of the Keithley device's light.

4. Challenges and Future Prospects

Despite the significant advancements achieved in dye-sensitized solar cell (DSSC) technology, large-scale commercialization is still hindered by several challenges, including limited long-term stability, charge recombination, restricted light absorption, and electrolyte leakage. Future research should focus on the development of highly stable nanostructured photoanodes, improvement of interfacial charge transfer, and the design of low-cost, environmentally friendly electrode materials with enhanced electrocatalytic activity. In

addition, the integration of carbon-based conductive materials, heterojunction nanocomposites, and surface defect engineering strategies may significantly improve solar energy conversion efficiency and electron transport properties. The practical applicability of DSSCs for sustainable solar energy conversion is expected to be further enhanced through advanced material optimization combined with scalable fabrication techniques[61].

5. Conclusion

Precipitation was used to create ZnO nanoparticles, ZnO/TiO_2, and ZnO/NiO nanocomposites. The efficiency of nanomaterials (semiconductors) in the creation of DSSCs has been studied, and ZnO nanoparticles, ZnO/TiO_2, and ZnO/NiO nanocomposites have been employed as electrodynamic catalysts. Because of its many features, including their compact size, surface area, and power output, solar cells are also used in everyday life. The study also demonstrates the potential for creating nanomaterials using a variety of techniques, including the straightforward chemical approach. to determine the transduction efficiency (η) of the blue dye in comparison to the red dye on DSSCs. It was investigated how produced ZnO nanoparticles and ZnO/TiO_2 and ZnO/NiO nanocomposites affected the conversion efficiency (η) using the red (cabbage) and blue (Brilliant Blue FCF-E133) dyes. Understanding the characteristics of nanomaterials' surfaces and their efficiency as photoelectrodes, in addition to their crystal structures and various forms, is one advantage of employing various characterizations. We also draw the conclusion that solar cells might be developed utilizing a variety of nanomaterials to enhance their electrical and functional characteristics and be used in the future to supply energy and power at the lowest possible cost. The size of the nanocrystals during the solid-to-solid phase transition has an impact on the functionality improvement in solar cells. Phase control is therefore a crucial step.

Conflict of interest

The authors declare no conflict of interest.

References

1. Y. Wu, C. Li, Z. Tian, J. Sun, Solar-driven integrated energy systems: State of the art and challenges, *J. Power Sources* 478 (2020) 228762.
2. N. Yan, C. Zhao, S. You, Y. Zhang, W. Li, Recent progress of thin-film photovoltaics for indoor application, *Chin. Chem. Lett.* 31 (3) (2020) 643–653.
3. R.A. Metwally, J. El Nady, S. Ebrahim, A. El Sikaily, N.A. El-Sersy, S.A. Sabry, H.A. Ghozlan, Biosynthesis, characterization and optimization of TiO_2 nanoparticles by novel marine halophilic *Halomonas* sp. RAM2: Application of natural dye-sensitized solar cells, *Microb. Cell Fact.* 22 (2023) 78.
4. S. Liu, J. Yuan, W. Deng, M. Luo, Y. Xie, Q. Liang, Y. Zou, Z. He, H. Wu, Y. Cao, High-efficiency organic solar cells with low non-radiative recombination loss and low energetic disorder, *Nat. Photonics* 14 (5) (2020) 300–305.
5. S.Y. Wang, C.P. Chen, C.L. Chung, C.W. Hsu, H.L. Hsu, T.H. Wu, J.Y. Zhuang, C.J. Chang, H.M. Chen, Y.J. Chang, Defect passivation by amide-based hole-transporting interfacial layer enhanced perovskite grain growth for efficient p–i–n perovskite solar cells, *ACS Appl. Mater. Interfaces* 11 (43) (2019) 40050–40061.
6. M.I. Omer, T. Ye, X. Li, S. Ma, D. Wu, L. Wei, X. Tang, S. Ramakrishna, Q. Zhu, S. Xiong, J. Xu, C. Vijila, X. Wang, Two quasi-interfacial p–n junctions observed by a dual-irradiation system in perovskite solar cells, *npj Flex. Electron.* 7 (2023) 23.
7. Y. Liao, N. Tian, J. Wang, D. Yao, G. Zheng, B. Zhou, Y. Yang, F. Long, Performance enhancement of evaporated $CsPbI_2Br$ perovskite solar cells with a CuSCN hole transport layer via a cesium bromide buffer layer, *ACS Appl. Energy Mater.* 5 (8) (2022) 9542–9548.
8. M.K. Mishu, M. Rokonuzzaman, J. Pasupuleti, M. Shakeri, K.S. Rahman, F.A. Hamid, S.K. Tiong, N. Amin, Prospective efficient ambient energy harvesting sources for IoT-equipped sensor applications, *Electronics* 9 (9) (2020) 1345.
9. M. Bardwell, J. Wong, S. Zhang, P. Musilek, Design considerations for IoT-based PV charge controllers, in: *Proc. IEEE World Congress on Services (SERVICES)*, 2018, pp. 59–60.
10. H. Michaels, M. Rinderle, R. Freitag, I. Benesperi, T. Edvinsson, R. Socher, A. Gagliardi, M. Freitag, Dye-sensitized solar cells under ambient light powering machine learning: Towards autonomous smart sensors for the Internet of Things, *Chem. Sci.* 11 (11) (2020) 2895–2906.

11. S. Dhingra, R.B. Madda, R. Patan, P. Jiao, K. Barri, A.H. Alavi, Internet of things-based fog and cloud computing technology for smart traffic monitoring, *Internet Things* 14 (2020) 100175.
12. H.K.H. Lee, J. Barbé, S.M.P. Meroni, T. Du, C.T. Lin, A. Pockett, J. Troughton, S.M. Jain, F. De Rossi, J. Baker, M.J. Carnie, M.A. McLachlan, T.M. Watson, J.R. Durrant, W.C. Tsoi, Outstanding indoor performance of perovskite photovoltaic cells – Effect of device architectures and interlayers, *Sol. RRL* 3 (1) (2019) 1800207.
13. K. Prajapat, M. Dhonde, K. Sahu, P. Bhojane, V.V.S. Murty, P.M. Shirage, The evolution of organic materials for efficient dye-sensitized solar cells, *J. Photochem. Photobiol. C* 55 (2023) 100586.
14. W.E. Meador, N.P. Liyanage, J. Watson, K. Groenhout, J.H. Delcamp, Panchromatic NIR-absorbing sensitizers with a thienopyrazine auxiliary acceptor for dye-sensitized solar cells, *ACS Appl. Energy Mater.* 6 (10) (2023) 5416–5428.
15. F. Perrella, X. Li, A. Petrone, N. Rega, Nature of the ultrafast interligand electron transfers in dye-sensitized solar cells, *JACS Au* 3 (1) (2023) 70–79.
16. D. Kumar, K.P.S. Parmar, P. Kuchhal, Optimizing photovoltaic efficiency of a dye-sensitized solar cell (DSSC) by a combined modelling–simulation and experimental study, *Int. J. Renew. Energy Res.* 10 (1) (2020) 165–174.
17. E. Supriyanto, H.A. Kartikasari, N. Alviati, G. Wiranto, Simulation of dye-sensitized solar cells (DSSC) performance for various local natural dye photosensitizers, *IOP Conf. Ser. Mater. Sci. Eng.* 515 (2019) 012048.
18. M.B.A. Bashir, A.H. Rajpar, E.Y. Salih, E.M. Ahmed, Preparation and photovoltaic evaluation of CuO@Zn(Al)O mixed metal oxides for dye-sensitized solar cell, *Nanomaterials* 13 (5) (2023) 802.
19. A. Alizadeh, M. Roudgar-Amoli, S.M. BonyadShekalgourabi, Z. Shariatinia, M. Mahmoudi, F. Saadat, Dye-sensitized solar cells go beyond using perovskite and spinel inorganic materials: A review, *Renew. Sustain. Energy Rev.* 157 (2022) 112047.
20. J. Lu, S. Liu, M. Wang, Push–pull zinc porphyrins as light-harvesters for efficient dye-sensitized solar cells, *Front. Chem.* 6 (2018) 541.
21. K. Kakiage, Y. Aoyama, T. Yano, K. Oya, J. Fujisawa, M. Hanaya, Highly-efficient dye-sensitized solar cells with collaborative sensitization by silyl-anchor and carboxy-anchor dyes, *Chem. Commun.* 51 (88) (2015) 15894–15897.
22. Y. Cao, Y. Liu, S.M. Zakeeruddin, A. Hagfeldt, M. Grätzel, Direct contact of selective charge extraction layers enables high-efficiency molecular photovoltaics, *Joule* 2 (2018) 1108–1117.
23. B. Boro, B. Gogoi, B.M. Rajbongshi, A. Ramchiary, Nano-structured TiO_2/ZnO nanocomposite for dye-sensitized solar cells application: A review, *Renew. Sustain. Energy Rev.* 81 (2018) 2264–2270.
24. J.A. Castillo-Robles, E. Rocha-Rangel, J.A. Ramírez-de-León, F.C. Caballero-Rico, Advances on dye-sensitized solar cells (DSSCs) nanostructures and natural colorants: A review, *J. Compos. Sci.* 5 (11) (2021) 288. https://doi.org/10.3390/jcs5110288.
25. K. Prajapat, U. Mahajan, K. Sahu, M. Dhonde, P.M. Shirage, The evolution of natural dye-sensitized solar cells: Current advances and future outlook, *Solar Energy* (2024).
26. P.S. Pawar, P.A. Koyale, S.S. Patil, S.R. Patil, J. Bae, N.R. Chodankar, Y.G. Kapdi, S.S. Soni, P.S. Patil, TiO_2/ZnO nanocomposites with a metal-free dye and a polymer gel electrolyte: Optimizing photovoltaic efficiency and assessing stability via time series analysis, *Energy Advances* (2025).
27. S. Haffad, Mechanism of the double heterostructure TiO_2/ZnO/TiO_2 for photocatalytic and photovoltaic applications: A theoretical study, arXiv:1702.02545 (2017).
28. M. Tokay, A.A. Oladipo, M. Kusaf, Octahedral-like $Ni_{0.3}Zn_{0.7}Fe_2O_4$–TiO_2 nanohybrid material as photoanode of natural dye-sensitized solar cells, *Opt. Mater.* 130 (2022) 112407.
29. M. Kandasamy, A. Husain, S. Suresh, J. Giri, D.J. Jasim, P. Rameshkumar, H.A. Al-Lohedan, Enhanced dye-sensitized solar cell performance and electrochemical capacitive behavior of bi-functional ZnO/NiO/Co_3O_4 ternary nanocomposite prepared by chemical co-precipitation method, *Mater. Today Commun.* 39 (2024) 100726.
30. H. Xu, N. Liang, L. Cui, H. Zhang, B. Yang, Z. Jin, Synergistic effect of interface and defect engineering of MoC/MoO_2 nano dot encapsulated N-doped carbon nanoflowers for highly durable dye-sensitized solar cells, *J. Colloid Interface Sci.* 653 (B) (2024) 1620–1629. https://doi.org/10.1016/j.jcis.2023.10.008.
31. S.M. Abu Nayem, S.S. Shah, S.B. Chaity, B.K. Biswas, B. Nahar, M.A. Aziz, M.Z. Hossain, Jute stick extract assisted hydrothermal synthesis of ZnO nanoflakes and their enhanced photocatalytic and antibacterial efficacy, *Arab. J. Chem.* 15 (11) (2022) 104265.
32. Y. Zhou, L. Xu, Z. Wu, P. Li, J. He, Optical and photocatalytic properties of nanocrystalline ZnO powders synthesized by a low-temperature hydrothermal method, *Optik* 130 (2017) 673–680.
33. R. Raji, K.G. Gopchandran, ZnO nanostructures with tunable visible luminescence: Effects of kinetics of chemical reduction and annealing, *J. Sci.: Adv. Mater. Devices* 2 (1) (2017) 51–58.
34. H. Selim, A.A. Nada, M. El-Sayed, R.M. Hegazey, E.R. Souaya, M.F. Kotkata, The effect of ZnO and its nanocomposite on the performance of dye sensitized solar cell, *Nano Sci. Nano Technol.* 12 (1) (2018) 122.
35. J.S. Khan, A. Radhakrishnan, B. Beena, Polyaniline/zinc oxide nanocomposite as antimicrobial agent, *Indian J. Adv. Chem. Sci.* 6 (2) (2018) 71–76.
36. T.W. Quadri, L.O. Olasunkanmi, O.E. Fayemi, M.M. Solomon, E.E. Ebenso, Zinc oxide nanocomposites of selected polymers: Synthesis, characterization, and corrosion inhibition studies, *ACS Omega* 2 (11) (2017) 8421–8437.

37. J. Revathi, M.J. Abel, V. Archana, T. Sumithra, R. Thiruneelakandan, J. Joseph Prince, Synthesis and characterization of $CoFe_2O_4$ and Ni-doped $CoFe_2O_4$ nanoparticles by chemical co-precipitation technique for photo-degradation of organic dyestuffs under direct sunlight, *Physica B* 587 (2020) 412136. https://doi.org/10.1016/j.physb.2020.412136. *(no corresponding record issue noted in review systems)*
38. Synthesis of ZnO/NiO/g-C_3N_4 nanocomposite materials for photocatalytic degradation of tetracycline antibiotic, (2023). *(Incomplete reference – needs journal, authors, DOI)*
39. J.V. González-Fernández, D.D. Pinzón-Moreno, A.A. Neciosup-Puican, M.V. Carranza-Oropeza, Green method, optical and structural characterization of ZnO nanoparticles synthesized using leaves extract of *M. oleifera*, *JRM* 10 (3) (2022).
40. B.S. Hulbert, W.M. Kriven, Specimen-displacement correction for powder X-ray diffraction in Debye–Scherrer geometry, *J. Appl. Crystallogr.* 56 (1) (2023).
41. N. Saxena et al., Equimolar ZnO–CdS nanocomposite for enhanced photocatalytic performance, *Chem. Phys. Impact* 5 (2022) 100119.
42. P. Basnet, D. Samanta, T.I. Chanu, J. Mukherjee, S. Chatterjee, Assessment of synthesis approaches for tuning photocatalytic properties of ZnO nanoparticles, *SN Appl. Sci.* (2019).
43. B.D. Cullity, S.R. Stock, *Elements of X-Ray Diffraction*, 3rd ed., Prentice Hall, 2001.
44. A.L. Patterson, The Scherrer formula for X-ray particle size determination, *Phys. Rev.* 56 (1939) 978–982.
45. S. Athithya, S. Harish, H. Ikeda, M. Navaneethan, J. Archana, Controlled synthesis of monodispersed ZnO nanospindle decorated TiO_2 mesospheres for enhanced charge transport in dye-sensitized solar cells, *CrystEngComm* 25 (2023) 3198–3210.
46. K. Davis, R. Yarbrough, M. Froeschle, J. White, H. Rathnayake, Band gap engineered zinc oxide nanostructures via sol–gel synthesis of solvent-driven shape-controlled crystal growth, *RSC Adv.* 9 (26) (2019) 14638–14648.
47. Plant-mediated Z-scheme ZnO/TiO_2 nanocomposites for antibacterial potential and dye degradation: Experimental and DFT study, (2024). *(Incomplete reference – missing journal/DOI)*
48. Using ZnO, NiO, and ZnO/NiO as nano photocatalyst for removal of Acid Violet and Rhodamine B from wastewater, *J. Nanostruct.* 12 (3) (2022) 761–770.
49. B. O'Regan, M. Grätzel, A low-cost, high-efficiency solar cell based on dye-sensitized colloidal TiO_2 films, *Nature* 353 (1991) 737–740.
50. A. Hagfeldt, G. Boschloo, L. Sun, L. Kloo, H. Pettersson, Dye-sensitized solar cells, *Chem. Rev.* 110 (2010) 6595–6663.
51. Q. Zhang, C.S. Dandeneau, X. Zhou, G. Cao, ZnO nanostructures for dye-sensitized solar cells, *Adv. Mater.* 21 (2009) 4087–4108.
52. M. Grätzel, Recent advances in sensitized mesoscopic solar cells, *Acc. Chem. Res.* 42 (11) (2009) 1788–1798.
53. K. Mahmood, B.S. Swain, A. Amassian, Highly efficient hybrid solar cells based on ZnO nanostructures, *Adv. Energy Mater.* 5 (2015).
54. M.A. Nasution, Iwantono, P. Nurrahmawati, et al., The enhancement light absorption of ZnO–TiO_2 nanocomposite as photoanode, *Int. J. Nanoelectron. Mater.* 16 (4) (2024) 883–890.
55. F.-I. Lai, J.-F. Yang, Y.-C. Hsu, et al., Enhancing DSSC performance through manipulation of the size of ZnO nanorods, *ACS Omega* 8 (43) (2023) 40206–40211.
56. C. Nizamudeen, R. Krishnapriya, M.S. Mozumder, et al., Photovoltaic performance of MOF-derived transition metal doped titania-based photoanodes for DSSCs, *Sci. Rep.* 13 (2023) 6345.
57. L. Schöttner, A. Nefedov, C. Yang, S. Heissler, Y. Wang, C. Wöll, Structural evolution of α-Fe_2O_3 (0001) surfaces under reduction conditions, *Front. Chem.* 7 (2019) 451.
58. Y. Fang, P. Ma, H. Cheng, G. Tan, J. Wu, J. Zheng, X. Zhou, S. Fang, Y. Dai, Y. Lin, Synthesis of low-viscosity ionic liquids for application in dye-sensitized solar cells, *Chem. Asian J.* 14 (23) (2019) 4201–4206.
59. D. Rangel, J.C. Gallegos, S. Vargas, F. García, R. Rodríguez, Optimized dye-sensitized solar cells: A comparative study with different dyes, mordants and construction parameters, *Results Phys.* 12 (2019) 2026–2037.
60. A.-S. Al-Hachamy, Preparation of high activity binary and ternary MgO nanocomposite catalysts and their environmental application, PhD Dissertation, University of Kufa, 2020.
61. S. Qamar, S.E. Ela, Dye-sensitized solar cells (DSSC): Principles, materials and working mechanism, *Curr. Opin. Colloid Interface Sci.* 76 (2024) 101871.